

Hidden AGNs in Early-Type Galaxies

Alessandro Paggi¹, Giuseppina Fabbiano¹, Francesca Civano^{1,2}, Silvia Pellegrini³, Martin Elvis¹ and Dong-Woo Kim¹

¹*Harvard-Smithsonian Center for Astrophysics, 60 Garden St, Cambridge, MA 02138, USA:*
apaggi@cfa.harvard.edu

²*Department of Physics and Yale Center for Astronomy and Astrophysics, Yale University, P.O. Box 208121, New Haven, CT 06520-8121*

³*Department of Astronomy, University of Bologna, via Ranzani 1, 40127 Bologna, Italy*

ABSTRACT

We present a stacking analysis of the complete sample of Early Type Galaxies (ETGs) in the *Chandra* COSMOS (C-COSMOS) survey, to explore the nature of the X-ray luminosity in the redshift and stellar luminosity ranges $0 < z < 1.5$ and $10^9 < L_K/L_\odot < 10^{13}$. Using established scaling relations, we subtract the contribution of X-ray binary populations, to estimate the combined emission of hot ISM and AGN. To discriminate between the relative importance of these two components, we (1) compare our results with the relation observed in the local universe $L_{X,gas} \propto L_K^{4.5}$ for hot gaseous halos emission in ETGs, and (2) evaluate the spectral signature of each stacked bin. We find two regimes where the non-stellar X-ray emission is hard, consistent with AGN emission. First, there is evidence of hard, absorbed X-ray emission in stacked bins including relatively high z (~ 1.2) ETGs with average high X-ray luminosity ($L_{X-LMXB} \gtrsim 6 \times 10^{42}$ erg/s). These luminosities are consistent with the presence of highly absorbed "hidden" AGNs in these ETGs, which are not visible in their optical-IR spectra and spectral energy distributions. Second, confirming the early indication from our C-COSMOS study of X-ray detected ETGs, we find significantly enhanced X-ray luminosity in lower stellar mass ETGs ($L_K \lesssim 10^{11} L_\odot$), relative to the local $L_{X,gas} \propto L_K^{4.5}$ relation. The stacked spectra of these ETGs also suggest X-ray emission harder than expected from gaseous hot halos. This emission is consistent with inefficient accretion $10^{-5} - 10^{-4} \dot{M}_{Edd}$ onto $M_{BH} \sim 10^6 - 10^8 M_\odot$.

Subject headings: galaxies: elliptical - surveys - X-rays: galaxies

1. Introduction

Diffuse X-ray emission from early type galaxies (ETG) has been observed since the *Einstein* X-ray Observatory era (Trinchieri & Fabbiano 1985; Forman et al. 1985). The nature of this emission was debated, because with the arcminute resolution of *Einstein* data it was not possible to disentangle in a direct observational way hot gas halos from discrete X-ray sources (e.g. low-mass X-ray binaries, LMXBs, Trinchieri & Fabbiano 1985). Several authors discussed how this emission and the inferred hot gas contribution could be used to constrain physical models of halo evolution, including feedback from SNIa and AGNs, and interaction with intracluster and group media (see e.g., Fabbiano 1989; Canizares et al. 1987; Ciotti et al. 1991; David et al. 1991; White & Sarazin 1991; Mathews & Brighenti 2003; Ciotti & Ostriker 2007).

Thanks to the high spatial resolution of *Chandra* and imaging/spectral capabilities of the ACIS detector (Garmire et al. 2003), it has become possible to discriminate between the different contributions to X-ray emission of ETGs. The presence of LMXB populations has been definitely proven, and these sources have been detected and studied in numerous ETGs to distances of several tens of megaparsecs (see e.g. Fabbiano 2006). The determination of the LMXB luminosity function in nearby ETGs (e.g., Kim & Fabbiano 2004; Gilfanov 2004; Kim et al. 2009), allowed Boroson et al. (2011, BKF11) to accurately estimate the gaseous contribution to the X-ray luminosity $L_{X,gas}$ of a sample of 30 nearby (within 32 Mpc) ETGs. BKF11 found steep relations between $L_{X,gas}$ and both the stellar L_K luminosity and the hot gas temperature T . Subsequent work by Kim & Fabbiano (2013, KF13; 2015, KF15) suggests that for $L_{X,gas} > 10^{40}$ erg s⁻¹ the hot gas around ETGs is virialized, giving a new way to measure the total mass of these galaxies.

Recently, Civano et al. (2014, C14) studied a sample of 69 X-ray detected ETGs in the *Chandra*-COSMOS survey (C-COSMOS, Elvis et al. 2009) covering a redshift range $0 < z < 1.5$ to extend to higher redshift the sample of ETGs and explore redshift dependencies in the BKF11, KF13 scaling relations. In particular, C14 focused on the relation between $L_{X,gas}$ and the K-band stellar luminosity (L_K) of ETGs. The latter has been evaluated in the local Universe by BKF11 as $L_{X,gas} \propto L_K^{2.6 \pm 0.4}$ for sources with $L_{X,gas} \leq 2 \times 10^{41}$ erg s⁻¹, while including sources with $L_{X,gas}$ up to 9×10^{42} erg s⁻¹ KF13 found a steeper $L_{X,gas} \propto L_K^{4.5 \pm 0.8}$ relation. C14 found that this latter relation also holds for X-ray detected ETGs with $L_{X,gas} \leq 10^{42}$ erg s⁻¹, suggesting that the hot gas in these more distant galaxies may be virialized as well. However, more distant ($z > 0.9$) and younger stellar age galaxies generally fall outside the relation observed in the local sample, and are X-ray overluminous with respect to their L_K . For these sources C14 suggested that the higher X-ray luminosity may be due to the presence of hidden AGNs (as suggested by observed hardness ratios), merging phenomena (which are expected to increase the halo X-ray luminosity Cox et al. 2006) or nuclear accretion (that could also induce AGN activity during the merging phase Cox et al. 2006)

In this work we perform a stacking analysis of the C-COSMOS data in order to investigate the nature of fainter, X-ray undetected ETGs, and compare their properties with those of the sample of local ETGs investigated by BKF11 and KF13, and of the sample of ETGs detected in the C-COSMOS survey studied by C14.

The paper is organized as follows: Section 2 describes the sample selection and the data sets used in this work, Section 3.3 is dedicated to the description of the adopted stacking procedure, in Section 4 we discuss our results, and Section 5 is dedicated to our conclusions. In the following, we adopt the standard flat cosmology with $\Omega_\Lambda = 0.73$ and $H_0 = 70$ km s⁻¹ Mpc⁻¹.

2. Sample Selection

The COSMOS survey (Scoville et al. 2007) provides a multi-wavelength characterization of over 1.5 million galaxies at redshift extending out to 5 in 2 deg² of the sky. The *Chandra* X-ray coverage (C-COSMOS Elvis et al. 2009) over 0.9 deg², gives us the means to study X-ray emission of ETGs, extending local studies to higher redshifts, and explore the redshift evolution of hot halos with large samples of galaxies.

Our ETG sample is selected from the most recent version of the COSMOS photometric catalog by Ilbert et al. (2009), which uses the most recent near-infrared photometry from the Ultra Deep Survey with the VISTA telescope (Ultra-VISTA McCracken et al. 2013), and presents other galaxy properties (stellar mass, age and star formation rate Ilbert et al. 2010). The spectral energy distribution (SED) identification performed by Ilbert et al. (2009) makes use of 7 elliptical galaxy templates with ages from 2 to 13 Gyr (Polletta et al. 2007). The SED templates were generated with the stellar population synthesis package developed by Bruzual & Charlot (2003), assuming an initial mass function from Chabrier (2003) and an exponentially declining star formation history. We selected galaxies classified as E or S0

and that have a reliable photometric redshift (Ilbert et al. 2009). In addition we selected only sources with Ultra-VISTA detection both in J and K bands, since these are needed to evaluate the rest frame L_K (see below). This narrows our sample to 10,808 (the COSMOS ETG sample considered in C14). We then selected only the 6436 ETGs falling in the C-COSMOS field, and then excluded the 48 X-ray detected ETGs in common with the C-COSMOS identification catalog (Civano et al. 2012)¹. This leads us to our final sample of 6388 C-COSMOS ETGs - not detected in X-rays - which constitutes the starting point of the stacking analysis described in this paper.

Following C14 we evaluated the K band luminosity of our sources from the Ultra-VISTA K-band aperture magnitude of the COSMOS photometric catalog. To calculate the rest frame K band luminosities we assumed a power law spectrum $f_\nu \propto \nu^{-\alpha}$ with $\alpha = -(J - K)/\log(\nu_J/\nu_K)$ (where J and K are the AB magnitudes from the COSMOS photometric catalog and ν_J and ν_K are the corresponding frequencies), and express the rest frame luminosities in solar luminosity as $L_K = 10^{-(K+\text{ext}-5.19)/2.5} \times (1+z)^{\alpha-1} \times (D_L/10)^2$, where z is the photometric redshift from the COSMOS catalog, D_L is the luminosity distance expressed in parsecs, and ext is the aperture correction parameter computed from the FWHM measured for all the COSMOS extended sources in the Hubble ACS data.

The distributions of the physical parameters of the 6388 C-COSMOS ETGs are compared in Figure 1 with the entire 10,808 COSMOS ETG sample, demonstrating that the sample of ETGs not detected in X-ray is representative of COSMOS ETGs overall. Note that the luminosity threshold is a function of redshift because of the uniform magnitude limit of the Ultra-VISTA COSMOS survey ($K_s \sim 24$, McCracken et al. 2013). The specific star formation rate for the majority of the ETGs is in the regime where Ilbert et al. (2010) defines galaxies as quiescent, although higher star formation rate is observed in young ETGs. The properties (luminosity, mass, star formation rate and age) of the COSMOS ETGs are in agreement with those reported by (Moresco et al. 2013) for a sample of ETGs selected using multiple criteria (including color-color diagrams, spectra, star formation rate and SED classification). Masses and luminosities are in agreement with those of the K-selected elliptical galaxies of Jones et al. (2014), extracted from a small area of the COSMOS field.

3. Analysis and Results

Below we describe the procedures followed in our stacking analysis. The results are summarized in Tables 1 and 2.

3.1. Count Extraction at ETG Positions

We used all 49 C-COSMOS observations to evaluate source and background counts for our sample of ETGs, excluding data in the ACIS-I chip gaps. We also excluded data from X-ray detected sources removing counts within a 10'' radius of all sources in the C-COSMOS source identification catalog (Civano et al. 2012). We replaced the excluded counts by sampling the Poisson distribution of the pixel values nearby background regions with DMFILTH CIAO task². When a source lay in the field of view of more than one observation, we combined the data from the different observations using the prescriptions from Puccetti et al. (2009), excluding observations where the source was more than 8 arcmin off-axis from the aim point.

¹Note that we selected sources with photometric redshift estimate in the catalog by Ilbert et al. (2009), while C14 selected their sources to have a spectroscopic or photometric redshift estimates in the C-COSMOS identification catalog, so the sample of 69 ETGs selected by the latter authors is not fully contained in our sample.

²<http://cxc.harvard.edu/ciao/ahelp/dmfilth.html>

Due to the variation of the *Chandra* Point Spread Function (PSF) radius R_{PSF} ³, we used an extraction radius r_{ext} that was determined by the source position in each observation in order to extract an optimal fraction of X-ray photons from the diffuse halo. For sources with morphological information available in the *HST*-ACS catalog (Leauthaud et al. 2007) we adopted the source semi-major axes R as a measure of its physical extent. For sources with $R > R_{PSF}$ we adopted values of r_{ext} that was the convolution of R and R_{PSF} ; otherwise we adopted $r_{ext} = R_{PSF}$ as we did for sources without morphological information in *HST*-ACS catalog. The average exposure time for each source within the extraction circle, E , was then evaluated. The histogram of extracted ETG position counts is shown in Figure 2 (blue line).

3.2. Background Evaluation

To evaluate the background we extracted counts from an annulus centered on the source coordinates, with inner-radius $2r_{ext}$ and outer radius $4r_{ext}$. Due to the very low signal, the background represents the largest source of uncertainty in this kind of analysis. To estimate the systematic uncertainties introduced by the evaluation of the background, we compared the results of three different methods, obtaining consistent results. First we simply evaluated the background contribution to the total source counts from the mean count value of the pixels in the whole background annulus. Second, we adopted the clipping procedure of Willott (2011, method b), which evaluates the mean count value μ - and the standard deviation σ - of all pixels within a circle of radius $4r_{ext}$ around each source position and then sets all pixels with count value larger than $\mu + 3\sigma$ to μ . This method suppresses the noise in the background annulus, but also removes signal from the source⁴. Lastly, we divided the background annulus into eight 45 degree sectors, and excluded all the sectors in which the mean count value was larger than $\mu + 3\sigma$, thus excluding regions of higher background without removing signal from the source. The net counts N obtained with all three methods are consistent within statistics.

To test the robustness of our results we also extracted counts from positions on the sky offset from the ETG coordinates by random distances between 15'' and 30'' both in right ascension and declination. The net counts of the non-source positions are shown in Figure 2. They follow an approximatively Gaussian distribution centered on zero, as expected from background fluctuations, while the ETG counts show an excess of positive signal.

3.3. Stacking Procedure

To evaluate the count rate C for each stacked bin we stacked the observed source net counts N and exposure E to obtain $C = \sum_i N_i / \sum_i E_i$. From these counts we subtracted the expected contributions from stellar sources (LMXBs and Ultra Luminous X-ray sources, ULXs), and evaluated the average bin rest-frame X-ray luminosity as explained below. We corrected L_K to take into account the evolution of the stellar population (i.e., the fading effect, see C14). Note that, at a given redshift, younger galaxies have larger fading correction than older ones. To compare our results with those of KF13 and C14 we considered sources with $9 < \log(L_K) < 13$.

We constructed the stacks by binning in both L_K and z , to ensure that the binning scheme did not produce any significant bias on the results. For the L_K binning, we first divided our sample in four $\log(L_K)$ bins, 9 – 10, 10 – 11, 11 – 12 and 12 – 13. We then ordered the sources in each bin in increasing redshift, and progressively stacked them

³In the following we consider the *Chandra*-ACIS radius enclosing 90% of the energy.

⁴For the rare cases where $\mu + 3\sigma < 1$, only pixels with two or more counts were clipped.

until we reached a minimum signal to noise ratio of 3; if this 3σ threshold could not be reached we stacked the signal from all the remaining sources in the bin. For the z binning, we followed the same procedure, dividing the sample into three bins 0 – 0.5, 0.5 – 1 and 1 – 1.5, and then ordered the sources in each bin in increasing L_K .

3.4. Evaluation of Non-stellar L_X for Each Stacked Bin

To subtract the LMXB contribution from the total X-ray emission, we evaluated the average LMXB contribution to each bin using the 0.3-8 keV relation from [Fragos et al. \(2013\)](#), as in C14:

$$\log(L_{LMXB}/M_*) = 30.259 - 1.505 \times \log(\text{age}) - 0.421 \times \log^2(\text{age}) + 0.425 \times \log^3(\text{age}) + 0.135 \times \log^4(\text{age}), \quad (1)$$

where L_X is expressed in erg s^{-1} , M_* is the average stellar mass of the stacking bin expressed in solar masses and age is the average stellar age of the stacking bin expressed in Gyr. We also evaluated the contribution to X-ray luminosity from ULXs that could be present in the galaxies using the scaling relations from [Calzetti et al. \(2007\)](#) and [Mineo et al. \(2012\)](#) between the ULX luminosity and the galaxy star formation rate. ULX contribution is more than an order of magnitude smaller than L_{X-LMXB} even for the least luminous L_K bins.

We converted the average 0.3 – 8 keV LMXB luminosities in each bin to count rates in the 0.5 – 7 keV interval using a power law model with index $\Gamma = 1.8$ (consistent with the typical spectrum of LMXBs) and Galactic absorption $N_H = 2.6 \times 10^{20} \text{ cm}^{-2}$. For these parameters the conversion factor used from *Chandra* count rates to fluxes is $1.04 \times 10^{-11} \text{ erg cm}^{-2} \text{ s}^{-1} \text{ cts}^{-15}$. We then subtracted these count rates from the stacked signals and converted back the resulting count rates into luminosities using a model comprising Galactic N_H plus a thermal APEC component with temperature depending on the source total X-ray luminosity. We adopted $kT = 0.7, 1$ and 2 keV for X-ray luminosities of $L_X < 10^{41}$, $10^{41} < L_X < 10^{42}$ and $L_X > 10^{42} \text{ erg s}^{-1}$, respectively, following BKF11 and [Dai et al. \(2007\)](#). Finally, we K-corrected the luminosity to the 0.3 – 8 keV rest frame band. These LMXB-subtracted luminosities, that we indicate as L_{X-LMXB} , are expected to include the emission from the hot gaseous halos, but may also include a possible contribution from any AGN harbored within these ETGs.

Figure 3 shows the results in the $L_{X-LMXB} - L_K$ plane for both L_K and z binning (Left and Right panels, respectively). In both binning schemes the overall scatter plots are consistent, showing that we do not suffer from strong binning biases. By construction, the L_K -first binning provides information on the extreme redshift bins (both high and low), while the z -first binning covers more fully the L_K range. The bins are numbered in Figure 3, following Tables 1 and 2. We use different colors to visually divide the stacking bins into four groups: red, for bins X-ray over-luminous with respect to the local L_{X-LMXB} and L_K relation (BKF11, KF13, see C14); yellow, for X-ray under-luminous bins; and grey and green for bins following the local relation with L_{X-LMXB} lower and higher than $10^{41} \text{ erg s}^{-1}$, respectively.

3.5. Hardness Ratios

Hardness ratios (HRs) were evaluated to characterize the ETG average spectral properties. $HR = (H - S)/(H + S)$, where S is the soft 0.5 – 2 keV counts and H the hard 2 – 7 keV counts. These HRs are those of the LMXB-subtracted emission. The contributions of these sources were evaluated and subtracted by applying the procedure in Sect. 3.4 to each energy band.

⁵<http://cxc.harvard.edu/toolkit/pimms.jsp>

In Figure 4 we show the HRs for the stacking bins using the same color code as in Figure 3. We plot HR versus z in the Left panel, using the L_K -first binning, which gives a better z sampling. We plot HR versus L_K in the Right panel, using the z -first binning, to explore the L_K behavior. The left panel of Figure 4 shows a distinct clustering in HR- z space of bins from separate loci of the $L_{X-LMXB} - L_K$ plane, as shown by the clusters of different color points. The Right panel shows that ETGs with larger stellar mass (L_K) tend to have lower HR. Given the scaling relations of ETGs (BKF11; KF13; KF15), this could just reflect a relation with total binding mass, with more massive galaxies being more efficient at retaining large hot gaseous halos.

4. Discussion

Figure 5 summarizes our results in the $L_{X-LMXB}L_K$ plane and compares them with the COSMOS ETG X-ray detections (C14) and with the near universe ETG data (BKF11, KF13). We show the local KF13 relation with a solid line, and the scatter in this relation with the two dashed lines. These lines are chosen to pass through the points for the most $L_{X,gas}$ luminous source (M87) and the most L_K luminous source (NGC1316), respectively. The COSMOS stacked-ETG results are overall consistent with the C14 COSMOS detections, but significantly increase the coverage at lower stellar luminosities. While most of the detected signals are compatible with the local KF13 relation, there are several detections that lie both to the left and to the right side of it, that is, bins that appear to be respectively over and under-luminous in X-ray with respect to their L_K .

In Figure 5 we also show the hardness ratios for each stacked bin with lines with slopes proportional to HR . We find positive HRs (i.e., harder spectra) in stacked bins outside the dashed line on the left. These are the lower L_K galaxies with significant X-ray excess (the red points in Figure 4, see also C14). We also find hard $HR > 0$ in some points with $L_{X-LMXB} > 10^{41}$ erg s $^{-1}$ and $z > 1$ (the three top green points in Figure 4), to the left of the solid line.

Instead, lower HR ratios (i.e., softer spectra) are found in bins following the local relation (between the two dashed lines). This is especially so for those to the right of the solid line. This suggests that they have a larger than average hot gas content up to $z \sim 1$.

Figure 6 compares the HR- z scatter diagram with a set of spectral models. On the Left, we show the expected HRs for thermal APEC (dashed lines; from bottom to top, $kT = 0.7, 1, 2$ and 3 keV) and power-law models (solid lines; fixed slope $\Gamma = 2$ and increasing intrinsic absorption from bottom to top, $N_H = 0, 10^{21}, 10^{22}$ and 10^{23} cm $^{-2}$). The APEC models are the expected emission of thermal gaseous emission, while the power-law models are typical AGN spectra. To illustrate cases of mixed emission from a hot gas component and a heavily obscured AGN, on the Right panel of Figure 6 we plot composite models consisting of $kT = 1$ keV APEC emission with line of sight N_H plus power-law models with slope $\Gamma = 2$ and intrinsic absorption $N_H = 10^{23}$ cm $^{-2}$. From the bottom to the top the relative normalization of the two models varies, to reflect an increasing contribution of the power-law model to the total flux, ranging from $\sim 0.2\%$ to $\sim 100\%$.

The X-ray over-luminous bins (red points) have generally high HRs consistent with being dominated by AGN emission, either with “normal” AGNs with absorbing columns $\gtrsim 10^{22}$ cm $^{-2}$, or in the case of the composite gas + AGN emission even highly obscured Compton Thick AGNs ($N_H > 10^{24}$ cm $^{-2}$, Risaliti et al. 1999; Levenson et al. 2006; Lehmer et al. 2010).

The bins following the local relation with $L_{X-LMXB} < 10^{41}$ erg s $^{-1}$ (grey points) show generally lower $HR < 0$ with respect to the over-luminous X-ray bins. Although these HRs suggest the presence of softer gaseous emission, they are not consistent with pure gaseous emission. These HRs are best explained with a combination of thermal and AGN emission. The composite models of Figure 6 Right would imply AGN components accounting on average for

15% – 62% of the X-ray luminosity. Given the X-ray luminosities of this subsample (Figures 3, 5), these ratios would imply average AGN luminosities ranging from $\sim 5 \times 10^{39}$ erg s $^{-1}$ to $\sim 5 \times 10^{40}$ erg s $^{-1}$. Considering our simple model assumptions, this may be consistent with the result of the near universe sample (BKF11), where low-luminosity X-ray sources are detected with Chandra with luminosities ranging from $\sim 10^{38}$ erg s $^{-1}$ to $\sim 5 \times 10^{41}$ erg s $^{-1}$.

The bins with $L_{X-LMXB} > 10^{41}$ erg s $^{-1}$ (green points) have hard $HR > 0$ incompatible with a low absorption power-law model (e.g., bins 21, 22 and 25). The three highest redshift bins in this group (e.g., bins 28, 29 and 30) have even harder $HR > 0.5$ that are compatible only with absorbing columns larger than 10^{23} cm $^{-2}$. This suggests that these galaxies harbor (on average) highly obscured Compton Thick AGNs that dominate their X-ray luminosity.

In summary, our stacking analysis suggests that on average AGN emission is likely to be present in ETGs. These AGNs may be faint and hidden in hot gas dominated ETGs, which are consistent with the near Universe scaling relation of virialized halos (KF13, KF15, see C14). In contrast, AGN emission appears to dominate the non-stellar X-ray emission in two classes of ETGs: (1) low-stellar mass ETGs ($\log(L_K/L_\odot) \lesssim 10.5$), and (2) higher redshift ETGs ($z > 0.5, > 1$) especially those overluminous in X-rays relative to the near universe $L_{X-LMXB} - L_K$ scaling relation. The latter group has HR values suggesting highly absorbed Compton Thick AGNs. We note that these AGNs were not visible in the COSMOS colors and spectra, since AGNs were excluded in our ETG sample selection process (C14).

4.1. Accretion Regimes for the AGNs

Figure 7 shows the results of the L_K -first stacking, with L_{-LMXB} plotted against stellar mass M_* and the mass of the nuclear black hole, M_{BH} . M_* was taken from COSMOS catalog, and M_{BH} was obtained from the $M_{BH} - M_*$ relation of McConnell & Ma (2013). Alternatively, one could derive M_{BH} from the $M_{BH} - L_K$ relation from Graham (2007). We note, however, that latter black hole masses are ~ 0.5 dex larger than the former. Uncertainties in these estimate are typically of a factor of ~ 2 (Tremaine et al. 2002; Graham 2007) and evolution to $z \sim 1 - 2$ may provide a systematic black hole mass increase of a similar factor (Merloni et al. 2010). These effects will not change our conclusions in the wide range covered by Figure 7.

On the right hand axis we plot $L_{bol} = 10 L_{X-LMXB}$, an appropriate bolometric correction for low-luminosity AGNs that radiate at a few 10s % of L_{Edd} (Kollmeier et al. 2006; Steinhardt & Elvis 2010). Given this nominal L_{bol} we can plot diagonal lines of constant L_{bol}/L_{Edd} . These lines range from 10^{-2} to 10^{-6} L/L_{Edd} .

We see that the massive high L_{X-LMXB} galaxies (green points) and the low-mass X-ray overluminous (red points) galaxies have implied Eddington ratios in the 10^{-3} to 10^{-5} range. RIAFs are generally believed to apply to all black hole accretion below $10^{-2} L/L_{Edd}$, so we would expect all these sources to be RIAFs. If the bolometric correction for RIAFs is smaller than that considered here, as may well be the case (Narayan & Yi 1995), the L_{bol} values on the y-axis should be correspondingly lower (as the Eddington ratios on the currently plotted dashed lines).

Alternatively the true L_{bol} of the three high z bins of massive high L_{X-LMXB} galaxies (green points 28, 29, 30) could be greatly underestimated. The HRs of these bins also imply highly absorbed emission ($N_H > 10^{23}$ cm $^{-2}$, Figure 6). If these are then Compton Thick AGN they may have much larger intrinsic luminosities, with factors of 100 being quite plausible (e.g., Risaliti et al. 1999; Levenson et al. 2006). They would have intrinsic luminosities $L_{0.5-10 \text{ keV}} \sim 10^{45}$ erg s $^{-1}$ and L_{bol}/L_{Edd} in the $\sim 10^{-2}$ range, so that they could lie within the normal AGN regime. Measurements in the mid-IR would likely show a large excess of this luminosity in this case and so should be checked.

Instead the galaxies consistent with the local $L_K - L_{X-LMXB}$ gaseous relation (grey points), with X-ray colors suggesting thermal emission plus a possible AGN component, have smaller Eddington ratios $\sim 10^{-5}$ to 10^{-6} (these ratios of course assume that the entire emission is due to an AGN; as shown in Figure 6, the AGN component may

range from $\sim 15 - 60\%$).

We also plot in Figure 7 the predictions from Volonteri et al. (2011) of L_{X-LMXB} for three values of M_* for both efficient and radiatively inefficient accretion flows (RIAFs Narayan & Yi 1995).

These authors’ models use the stellar density profile scaling with stellar mass, and predict the accretion rate from the normal stellar mass loss due to stellar evolution, and the consequent massive black hole luminosity for various radiative efficiencies⁶. The X-ray luminosity coming from accretion is computed as $L_{X-LMXB}/L_{Edd} = \eta_X \eta \dot{m}$, where $\eta_X = 0.1$ is the X-ray fraction of the bolometric luminosity, and $\dot{m} = 0.1 \dot{M}/\dot{M}_{Edd}$ is the accretion rate in Eddington units with a 10% accretion efficiency. Radiatively efficient accretion flows have $\eta = 1$, while inefficient ones have $\eta = \dot{m}/\dot{m}_{cr}$, and for them $\dot{m} < \dot{m}_{cr} = 3 \times 10^{-2}$. In order to compare our results with Volonteri et al. (2011) models we converted the 0.3 – 8 keV luminosities into their 0.5 – 10 keV band, $L_{0.5-10 \text{ keV}}$, as described in Sect. 3.3. Based on these models, inefficient accretion into the nuclei could explain even all the L_{X-LMXB} of the massive, high L_{X-LMXB} ETGs (green points), except for the most luminous ones, which are likely to be Compton thick AGNs (see above). The low-mass X-ray overluminous ETGs (red points) are also consistent with the Volonteri et al. model. Considering that a large fraction of the X-ray emission is due to hot gas (see above), the grey points show instead a possible AGN emission even lower than predicted for radiatively inefficient accretion. In these ETGs, the L_{X-LMXB} is consistent with the local $L_{X,gas} - L_K$ relation. This result can have the following possible explanations, that are not mutually exclusive. The first is that the Volonteri et al.’s models assume that the whole of their estimated mass accretion rate (coming from the instantaneous mass loss of all stars, and obtained by integrating over the whole stellar density profile) indeed reaches the massive black hole, while this represents an upper limit on the mass accretion rate of the massive black hole (some gas may be outflowing, or may reach the massive black hole with a delay, or may possess angular momentum and form a disk, etc.). A second possibility is that the accreting mass, that has already entered the accretion radius, is reduced on its way to the massive black hole, due to a wind from a RIAF (Narayan & Yi 1995; Blandford & Begelman 1999); similarly, close to the nucleus, there may be a heating mechanism for the accreting gas, as a nuclear jet, again impeding or lowering the accretion rate (e.g. Pellegrini et al. 2012; Yuan & Li 2011). A third possibility is that accretion onto the black hole is (temporarily) not taking place, as may be the case during feedback-regulated activity cycles. Numerical simulations show that, during these cycles, AGN outbursts are followed by major degassing of the circumnuclear region, with a precipitous drop of the nuclear accretion rate; the outbursts are separated by long time intervals during which the galaxy is replenished again by gas from the stellar mass losses, until a new nuclear outburst takes place (Ciotti et al. 2010). A final possibility is that η_X might be lower than 1 as assumed here (see also Volonteri et al. 2011), or that η at low \dot{m} decreases faster than adopted in the Volonteri et al.’s models, so that lower L_{X-LMXB} should be predicted (e.g., Yuan & Narayan 2014).

Our results extend to higher X-ray luminosities a recent analysis of ETGs in the AMUSE survey of Virgo and field galaxies with *Chandra* (Miller et al. 2015). AMUSE results indicate a significant presence of supermassive black holes in low stellar mass galaxies. Due to the lower redshifts of the AMUSE ETGs that survey is sensitive to X-ray luminosities ($\sim 1.3 \times 10^{38}$ erg/s) one order of magnitude fainter are than our faintest bin 1 ($\sim 2.4 \times 10^{39}$ erg/s). For these dim sources the stellar wind accretion proposed by Volonteri et al. (2011) would predict higher X-ray luminosities than those observed. Miller et al. conclude that these black holes are probably powered by inefficient advection dominated accretion flows or, alternatively, by an outflow/jet component. We found that low-luminosity, X-ray “overluminous” ETGs can be adequately described by the RIAF fueled by stellar winds as proposed by Volonteri et al. (2011). Instead, ETGs with $L_{X-LMXB} > 10^{42}$ erg s⁻¹ may host Compton Thick AGNs.

⁶We note that in Volonteri et al. (2011) models assume for ETGs a stellar age of 12 Gyr. We corrected for the average age $10^{9.5}$ Gyr of C-COSMOS ETGs (see Figure 1), which yields slightly smaller emitted X-ray luminosities (see Eq. 9 in Volonteri et al. 2011).

5. Summary and Conclusions

We have followed up our previous work (C14) investigating the X-ray / K-band properties of the 69 ETGs detected in the Chandra COSMOS survey (Elvis et al. 2009), with a luminosity and hardness ratio stacking analysis of the *Chandra* data for the sample of 6388 early type galaxies (ETGs) not detected in X-rays. The stacking analysis allows the investigation of the average features of individually X-ray undetected ETGs. Our ETG sample was selected as representative of normal galaxies, with no evidence of AGN emission in their spectra and multi-band photometry (C14, Section 2). Our purpose was to investigate the properties of the X-ray emission from hot gas and from possible hidden AGN components that may be revealed by their X-ray emission. To this purpose, the expected contribution of LMXBs was subtracted from the X-ray luminosity of each stacked bin, using established scaling relations with the K-band luminosity (BKF11). All luminosities were corrected to the local rest frame; X-ray hardness ratios were based on the observed counts (after subtraction of the LMXB contribution), and were compared to emission models for the appropriate average bin redshift.

This analysis has led to the following conclusions:

1. On average AGN emission may be present in all ETGs.
2. AGNs may be faint and hidden in hot gas dominated ETGs, which are consistent with the local universe scaling relation of virialized halos (KF13, KF15, see C14).
3. AGN emission appears to dominate the non-stellar X-ray emission in low-stellar mass ETGs ($\log(L_K) \lesssim 10.5$ in solar units), which show marked X-ray luminosity excesses relative to their K-band luminosity (a proxy of stellar mass), when compared with the local ETG $L_{X,Gas}L_K$ relation of the local universe (BKF11). This result confirms the conclusions of C14 and extends them to lower stellar mass galaxies.
4. AGN emission is also prominent in higher redshift ETGs ($z > 0.5$, > 1) especially those with X-ray luminosity $\gtrsim 10^{42}$ erg s⁻¹. The latter group have HR values suggesting highly absorbed Compton Thick AGNs. We note that these AGNs were not visible in the COSMOS colors and spectra, since AGNs were excluded by our ETG sample (C14).
5. Given the nuclear BH mass predicted by the $M_{BH}-L_K$ relation (McConnell & Ma 2013), the hidden AGNs in the X-ray over-luminous low stellar mass ETGs are consistent with the presence of radiatively inefficient accretion fueled by stellar outgassing (Volonteri et al. 2011). The highly absorbed higher L_{X-LMXB} AGNs hidden in massive, higher z ETGs instead suggest efficient accretion in highly obscured nuclei.

This work was partially supported by NASA contract NAS8-03060 (CXC), and NASA Chandra grant G01-12110X. SP acknowledges financial support from MIUR grant PRIN 2010-2011, project ‘The Chemical and Dynamical Evolution of the Milky Way and Local Group Galaxies’, prot. 2010LY5N2T. FC acknowledges financial support by the NASA contract 11-ADAP11-0218. AP thanks Andy Goulding for useful discussion and suggestions. ME and GF thank the Aspen Center for Physics and the NSF Grant #1066293 for hospitality during the completion of this paper. This research has made use of software provided by the Chandra X-ray Center (CXC) in the application packages CIAO, ChIPS, and Sherpa. This research is based on observations collected at the European Organisation for Astronomical Research in the Southern Hemisphere, Chile, program 179.A-2005 (UltraVISTA survey).

REFERENCES

- Blandford, R. D., & Begelman, M. C. 1999, *MNRAS*, 303, L1
- Boroson, B., Kim, D.-W., & Fabbiano, G. 2011, *ApJ*, 729, 12
- Bruzual, G., & Charlot, S. 2003, *MNRAS*, 344, 1000
- Calzetti, D., Kennicutt, R. C., Engelbracht, C. W., et al. 2007, *ApJ*, 666, 870
- Canizares, C. R., Fabbiano, G., & Trinchieri, G. 1987, *ApJ*, 312, 503
- Chabrier, G. 2003, *PASP*, 115, 763
- Ciotti, L., D’Ercole, A., Pellegrini, S., & Renzini, A. 1991, *ApJ*, 376, 380
- Ciotti, L., & Ostriker, J. P. 2007, *ApJ*, 665, 1038
- Ciotti, L., Ostriker, J. P., & Proga, D. 2010, *ApJ*, 717, 708
- Civano, F., Elvis, M., Brusa, M., et al. 2012, *ApJS*, 201, 30
- Civano, F., Fabbiano, G., Pellegrini, S., et al. 2014, *ApJ*, 790, 16
- Cox, T. J., Di Matteo, T., Hernquist, L., et al. 2006, *ApJ*, 643, 692
- Dai, X., Kochanek, C. S., & Morgan, N. D. 2007, *ApJ*, 658, 917
- Danielson, A. L. R., Lehmer, B. D., Alexander, D. M., et al. 2012, *MNRAS*, 422, 494
- David, L. P., Forman, W., & Jones, C. 1991, *ApJ*, 369, 121
- Elvis, M., Civano, F., Vignali, C., et al. 2009, *ApJS*, 184, 158
- Fabbiano, G. 1989, *ARA&A*, 27, 87
- Fabbiano, G. 2006, *ARA&A*, 44, 323
- Forman, W., Jones, C., & Tucker, W. 1985, *ApJ*, 293, 102
- Fragos, T., Lehmer, B. D., Naoz, S., Zezas, A., & Basu-Zych, A. 2013, *ApJ*, 776, L31
- Garmire, G. P., Bautz, M. W., Ford, P. G., Nousek, J. A., & Ricker, G. R., Jr. 2003, *Proc. SPIE*, 4851, 28
- Gilfanov, M. 2004, *MNRAS*, 349, 146
- Graham, A. W. 2007, *MNRAS*, 379, 711
- Ilbert, O., Capak, P., Salvato, M., et al. 2009, *ApJ*, 690, 1236
- Ilbert, O., Salvato, M., Le Floch, E., et al. 2010, *ApJ*, 709, 644
- Jannuzi, B. T., & Dey, A. 1999, *Photometric Redshifts and the Detection of High Redshift Galaxies*, 191, 111
- Jones, T. M., Kriek, M., van Dokkum, P. G., et al. 2014, *ApJ*, 783, 25
- Kim, D.-W., & Fabbiano, G. 2004, *ApJ*, 611, 846

- Kim, D.-W., Fabbiano, G., Brassington, N. J., et al. 2009, *ApJ*, 703, 829
- Kim, D.-W., & Fabbiano, G. 2013, *ApJ*, 776, 116
- Kim, D.-W., & Fabbiano, G. 2015, arXiv:1504.00899
- Kochanek, C. S., Eisenstein, D. J., Cool, R. J., et al. 2012, *ApJS*, 200, 8
- Kollmeier, J. A., Onken, C. A., Kochanek, C. S., et al. 2006, *ApJ*, 648, 128
- Leauthaud, A., Massey, R., Kneib, J.-P., et al. 2007, *ApJS*, 172, 219
- Lehmer, B. D., Brandt, W. N., Alexander, D. M., et al. 2007, *ApJ*, 657, 681
- Lehmer, B. D., Alexander, D. M., Bauer, F. E., et al. 2010, *ApJ*, 724, 559
- Levenson N. A., Heckman T. M., Krolik J. H., Weaver K. A., Życki P. T., 2006, *ApJ*, 648, 111
- Mathews, W. G., & Brighenti, F. 2003, *ARA&A*, 41, 191
- McConnell, N. J., & Ma, C.-P. 2013, *ApJ*, 764, 184
- McCracken, H. J., Milvang-Jensen, B., Dunlop, J., et al. 2013, *The Messenger*, 154, 29
- Merloni, A., Bongiorno, A., Bolzonella, M., et al. 2010, *ApJ*, 708, 137
- Miller, B. P., Gallo, E., Greene, J. E., et al. 2015, *ApJ*, 799, 98
- Mineo, S., Gilfanov, M., & Sunyaev, R. 2012, *MNRAS*, 419, 2095
- Moresco, M., Pozzetti, L., Cimatti, A., et al. 2013, *A&A*, 558, A61
- Murray, S. S., Kenter, A., Forman, W. R., et al. 2005, *ApJS*, 161, 1
- Narayan, R., & Yi, I. 1995, *ApJ*, 452, 710
- Pellegrini, S., Wang, J., Fabbiano, G., et al. 2012, *ApJ*, 758, 94
- Polletta, M., Tajer, M., Maraschi, L., et al. 2007, *ApJ*, 663, 81
- Puccetti, S., Vignali, C., Cappelluti, N., et al. 2009, *ApJS*, 185, 586
- Risaliti, G., Maiolino, R., & Salvati, M. 1999, *ApJ*, 522, 157
- Scoville, N., Abraham, R. G., Aussel, H., et al. 2007, *ApJS*, 172, 38
- Steinhardt, C. L., & Elvis, M. 2010, *MNRAS*, 402, 2637
- Tremaine, S., Gebhardt, K., Bender, R., et al. 2002, *ApJ*, 574, 740
- Trinchieri, G., & Fabbiano, G. 1985, *ApJ*, 296, 447
- Tzanavaris, P., & Georgantopoulos, I. 2008, *A&A*, 480, 663
- Volonteri, M., Dotti, M., Campbell, D., & Mateo, M. 2011, *ApJ*, 730, 145
- Watson, C. R., Kochanek, C. S., Forman, W. R., et al. 2009, *ApJ*, 696, 2206

White, R. E., III, & Sarazin, C. L. 1991, *ApJ*, 367, 476

Willott, C. J. 2011, *ApJ*, 742, L8

Yuan, F., & Li, M. 2011, *ApJ*, 737, 23

Yuan, F., & Narayan, R. 2014, *ARA&A*, 52, 529

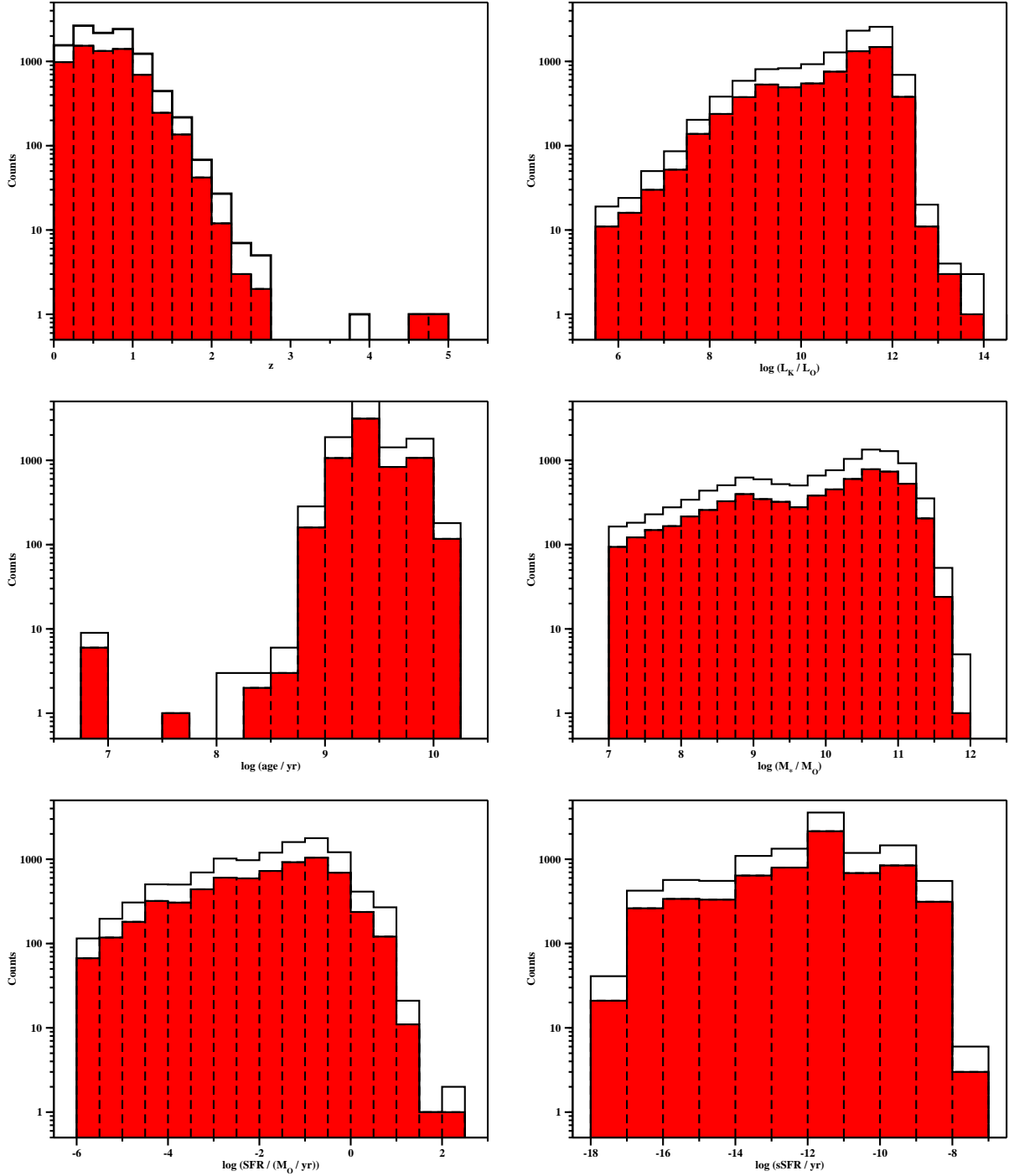


Fig. 1.— Histograms of the C-COSMOS ETGs sample studied in this work (red) compared with the entire COSMOS ETG sample (white). Top Left: redshift. Top right: rest frame L_K . Middle left: stellar age. Middle right: stellar mass. Bottom left: SFR. Bottom left: sSFR.

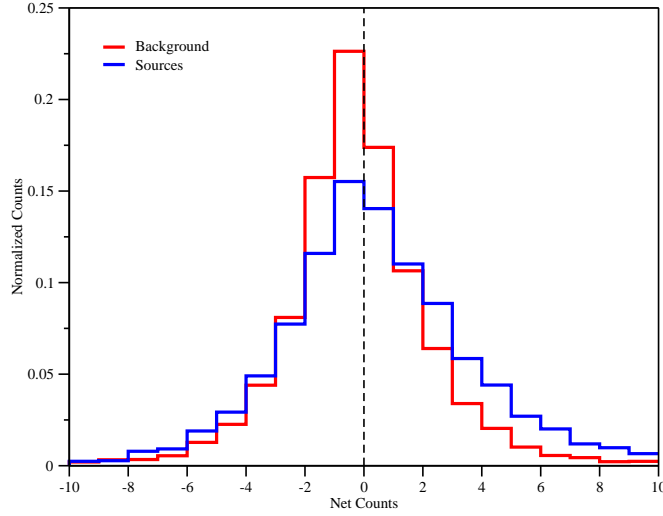


Fig. 2.— Distribution of net counts for randomly distributed extraction regions (red line) and for the selected sample of sources (blue line).

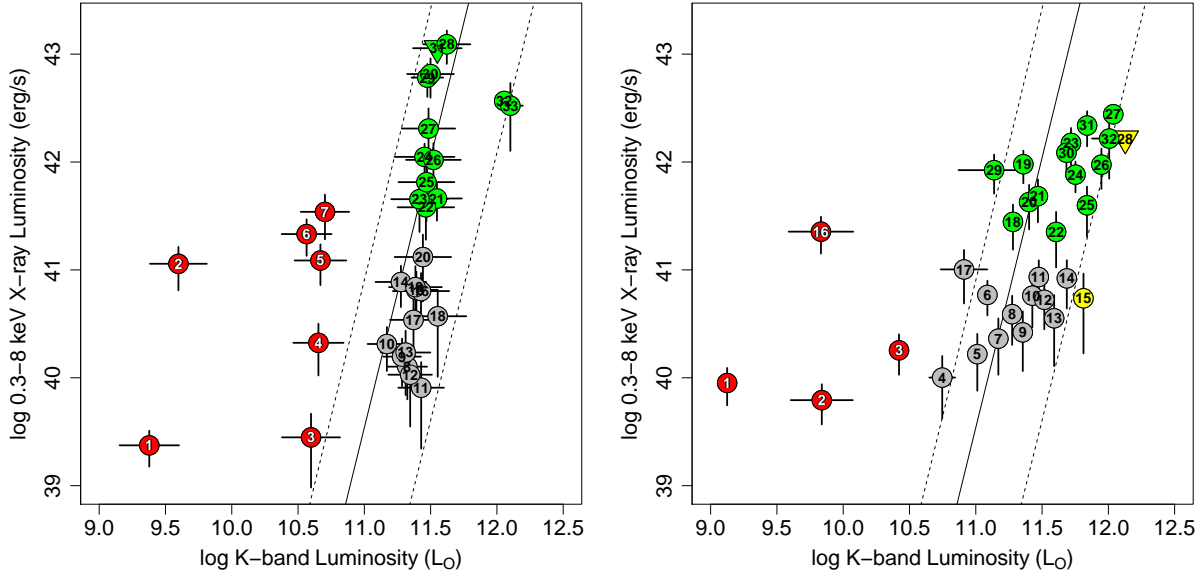


Fig. 3.— X-ray luminosity (after LMXBs subtraction) versus K-band luminosity for the stacking bins selected in L_K (Left Panel) and redshift (Right Panel). The horizontal and vertical error bars indicate the statistical uncertainties on L_K and L_{X-LMXB} , respectively. The local relation by KF13 is represented with a full black line. The dashed lines are drawn to include the most $L_{X, gas}$ luminous source ETG (M87) and the most L_K luminous ETG (NGC1316) in the Local Sample (BKF11, KF13), respectively. Bins are labelled as in Table 1 (for the left panel) and Table 2 (for the right panel): red, X-ray over-luminous with respect to the local $L_{X, gas} - L_K$ relation; yellow, X-ray under-luminous bins; grey and green bins following the local relation with L_{X-LMXB} lower and higher than 10^{41} erg s $^{-1}$, respectively. Triangles pointing down represent upper limits.

Table 1: Main features of the L_K selected stacking bins: (1) bin number; (2) number of stacked sources; (3) average rest frame L_K in the bin (with relative standard deviation); (4) average redshift in the bin (with relative standard deviation); (5) signal to noise ration of the stacked signal; (6) average 0.3-8 X-ray luminosity after LMXB subtraction (with relative uncertainties due to standard deviation of counts in the bin and to standard deviation of redshift in the bin); (7) hardness ratio (with relative error).

bin number	number of sources	$\langle \log(L_K/L_\odot) \rangle$	$\langle z \rangle$	S/N	$\langle L_{X-LMXB}/(10^{40} \text{ erg cm}^{-2} \text{ s}^{-1}) \rangle$	HR
1	93	9.38(0.22)	0.16(0.04)	3.12	0.24(0.09,0.12)	0.32(0.32)
2	946	9.60(0.21)	0.62(0.34)	2.60	11.40(4.94,10.72)	0.18(0.40)
3	272	10.60(0.22)	0.27(0.07)	3.09	0.28(0.18,0.15)	0.12(0.32)
4	190	10.65(0.19)	0.38(0.02)	3.00	2.11(1.06,0.26)	0.11(0.39)
5	41	10.67(0.19)	0.44(0.01)	3.01	12.23(5.01,0.73)	0.10(0.38)
6	43	10.56(0.19)	0.48(0.01)	3.24	21.48(7.99,0.67)	0.49(0.32)
7	1017	10.70(0.18)	0.80(0.19)	3.03	34.53(15.33,8.27)	0.23(0.30)
8	4	11.32(0.15)	0.18(0.01)	3.14	1.27(0.64,0.15)	-0.05(0.33)
9	7	11.28(0.14)	0.21(0.01)	3.12	1.57(0.73,0.06)	-0.13(0.40)
10	7	11.17(0.15)	0.22(0.01)	3.02	2.06(0.90,0.01)	< -0.11
11	20	11.43(0.17)	0.24(0.02)	3.24	0.81(0.59,0.12)	-0.60(0.36)
12	43	11.35(0.16)	0.29(0.02)	3.06	1.07(0.71,0.13)	-0.30(0.34)
13	59	11.31(0.19)	0.34(0.01)	3.21	1.71(1.02,0.12)	< -0.19
14	13	11.28(0.19)	0.35(0.01)	3.12	7.73(3.21,0.16)	0.32(0.38)
15	13	11.39(0.16)	0.36(0.01)	3.04	6.53(3.09,0.01)	-0.03(0.34)
16	16	11.43(0.21)	0.37(0.01)	3.04	6.36(3.00,0.15)	0.21(0.33)
17	45	11.37(0.18)	0.38(0.01)	3.05	3.44(2.06,0.08)	-0.48(0.47)
18	45	11.55(0.22)	0.39(0.01)	3.03	3.72(2.70,0.13)	-0.54(0.43)
19	91	11.39(0.20)	0.45(0.03)	3.09	6.92(3.87,0.90)	-0.06(0.41)
20	216	11.44(0.21)	0.59(0.06)	3.04	13.16(8.06,2.25)	-0.41(0.39)
21	27	11.55(0.19)	0.67(0.01)	3.30	45.92(17.3,0.06)	0.18(0.38)
22	161	11.46(0.21)	0.69(0.01)	3.06	38.05(19.03,0.80)	0.09(0.38)
23	238	11.42(0.21)	0.75(0.04)	3.27	45.23(22.76,2.60)	-0.49(0.46)
24	59	11.45(0.23)	0.83(0.01)	3.78	111.59(36.55,0.30)	-0.38(0.16)
25	319	11.47(0.21)	0.86(0.02)	3.04	65.09(36.91,1.05)	0.38(0.33)
26	122	11.52(0.21)	0.93(0.01)	3.25	104.73(44.55,1.54)	-0.39(0.42)
27	565	11.48(0.20)	1.06(0.08)	3.04	204.40(109.67,8.52)	< -0.09
28	24	11.62(0.18)	1.20(0.01)	3.26	1234.10(422.67,1.25)	< 0.52
29	3	11.48(0.12)	1.21(0.01)	3.09	606.33(204.04,0.14)	0.66(0.29)
30	112	11.50(0.18)	1.25(0.04)	3.02	653.77(259.30,13.42)	0.55(0.31)
31	80	11.55(0.18)	1.40(0.04)	1.29	< 1134.83	-0.05(0.90)
32	8	12.05(0.03)	0.66(0.09)	6.55	368.43(61.58,100.30)	-0.24(0.16)
33	27	12.10(0.09)	1.09(0.18)	2.31	332.98(206.20,50.76)	-0.37(0.54)

Table 2: Same as Table 1 but for redshift selected stacking bins.

bin number	number of sources	$\langle \log(L_K/L_\odot) \rangle$	$\langle z \rangle$	S/N	$\langle L_{X-LMXB}/(10^{40} \text{ erg cm}^{-2} \text{ s}^{-1}) \rangle$	HR
1	186	9.12(0.07)	0.29(0.10)	3.02	0.90(0.34,0.68)	0.53(0.32)
2	511	9.84(0.23)	0.31(0.10)	3.03	0.62(0.25,0.42)	-0.34(0.47)
3	129	10.42(0.06)	0.34(0.10)	3.07	1.80(0.73,1.15)	0.54(0.35)
4	241	10.75(0.10)	0.35(0.08)	3.01	1.00(0.59,0.53)	-0.07(0.36)
5	97	11.01(0.04)	0.35(0.08)	3.11	1.66(0.90,0.88)	0.35(0.30)
6	9	11.09(0.01)	0.32(0.08)	3.38	5.87(2.08,3.47)	-0.07(0.33)
7	91	11.17(0.04)	0.36(0.07)	3.06	2.31(1.24,1.00)	< -0.36
8	37	11.27(0.02)	0.36(0.07)	3.06	3.89(1.87,1.90)	-0.06(0.35)
9	46	11.35(0.03)	0.35(0.07)	3.03	2.64(1.49,1.20)	< -0.35
10	25	11.43(0.02)	0.37(0.07)	3.02	5.77(2.83,2.53)	> 0.30
11	20	11.48(0.01)	0.38(0.07)	3.10	8.59(3.67,3.47)	-0.38(0.40)
12	18	11.52(0.02)	0.36(0.07)	3.25	5.29(2.47,2.57)	-0.16(0.32)
13	28	11.59(0.03)	0.36(0.07)	3.05	3.56(2.28,1.64)	-0.46(0.48)
14	13	11.69(0.02)	0.37(0.06)	3.13	8.35(3.96,2.92)	< -0.40
15	18	11.81(0.05)	0.38(0.06)	3.05	5.46(3.77,1.91)	-0.18(0.33)
16	425	9.83(0.24)	0.73(0.14)	3.02	22.62(8.46,10.53)	0.51(0.35)
17	1159	10.91(0.18)	0.77(0.13)	3.07	10.10(5.22,4.33)	-0.10(0.36)
18	262	11.28(0.04)	0.79(0.13)	3.03	27.90(12.48,11.00)	-0.35(0.34)
19	34	11.36(0.01)	0.82(0.14)	3.30	95.44(31.98,38.48)	0.07(0.31)
20	111	11.40(0.02)	0.81(0.14)	3.04	42.58(18.87,17.86)	0.09(0.35)
21	106	11.47(0.02)	0.81(0.14)	3.08	48.30(20.72,19.73)	0.32(0.34)
22	274	11.61(0.05)	0.80(0.14)	3.07	22.51(11.99,9.37)	0.09(0.35)
23	8	11.72(0.01)	0.77(0.10)	3.17	150.53(56.56,48.19)	0.13(0.34)
24	51	11.75(0.02)	0.79(0.15)	3.78	76.48(24.10,34.97)	< -0.62
25	86	11.84(0.04)	0.81(0.14)	3.03	39.71(19.45,16.23)	< -0.17
26	28	11.95(0.02)	0.85(0.12)	3.24	94.64(38.33,33.54)	-0.02(0.34)
27	15	12.04(0.02)	0.81(0.16)	6.03	277.27(51.58,132.98)	-0.31(0.19)
28	8	12.13(0.03)	0.86(0.16)	1.20	< 197.66	< 0.68
29	737	11.14(0.27)	1.18(0.12)	3.06	84.07(33.16,21.52)	0.52(0.30)
30	127	11.68(0.06)	1.20(0.12)	3.25	122.08(48.68,30.32)	-0.26(0.38)
31	14	11.84(0.02)	1.25(0.15)	3.18	217.93(78.25,66.11)	-0.46(0.39)
32	33	12.01(0.13)	1.21(0.13)	2.32	165.07(95.09,42.85)	-0.35(0.54)

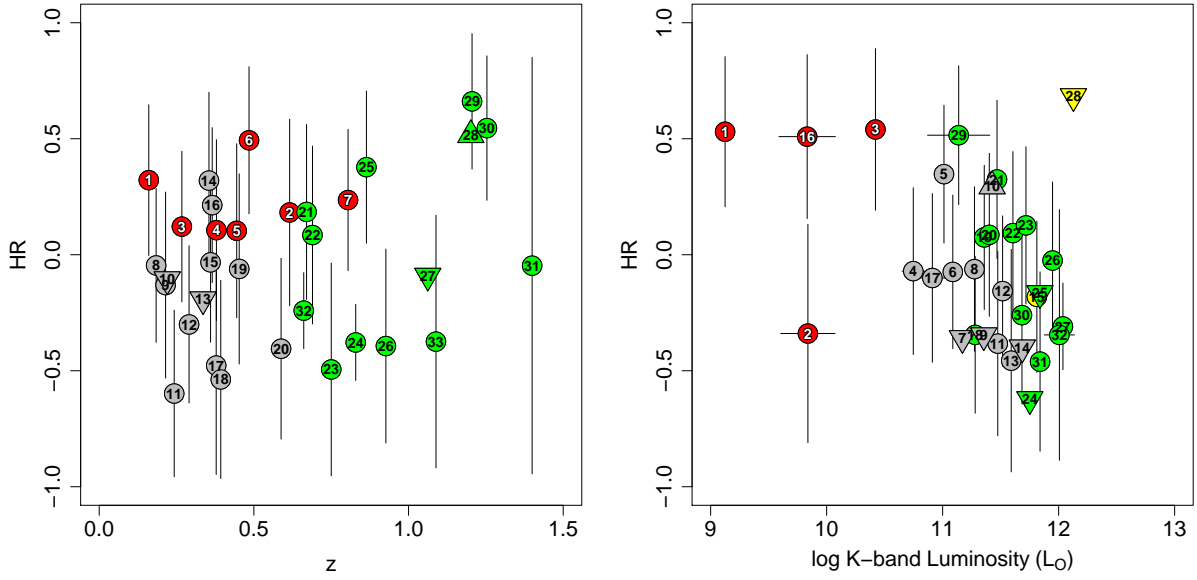


Fig. 4.— Left: HRs of the L_K -first stacking bins versus redshift. Right: HRs of the z -first stacking bins versus L_K . Triangles pointing up and down represent lower and upper limits on HR, respectively.

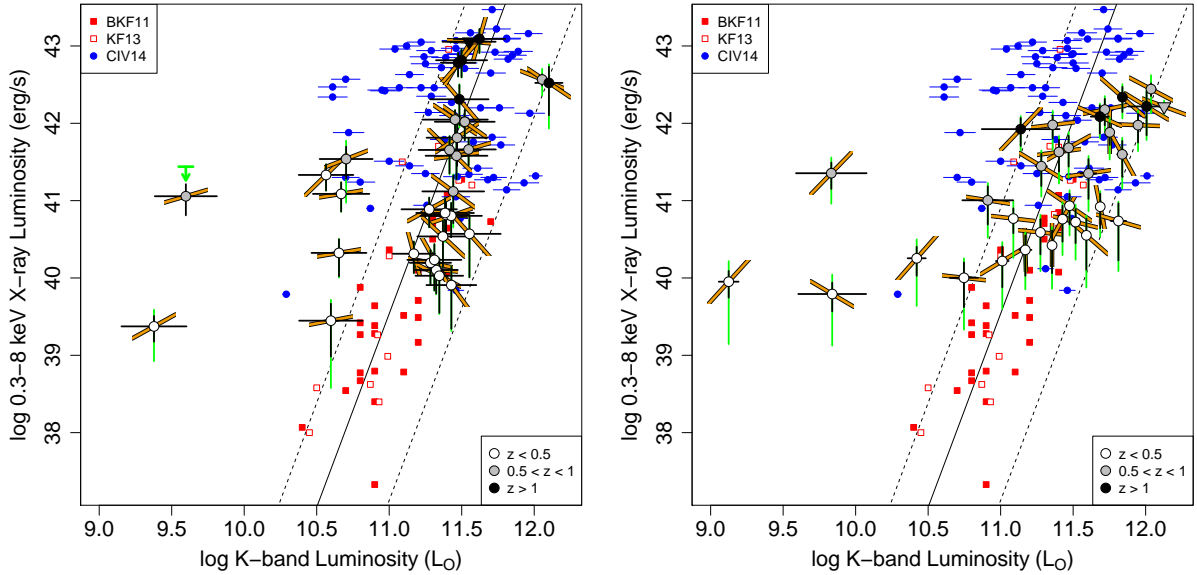


Fig. 5.— Same as Figure 3, but with bins labelled according to their average redshift, and HRs indicated by the slope of the orange segments. Black error bars reflect statistical uncertainties, vertical green bars show the uncertainty on L_{X-LMXB} due to redshift spread in each bin. Red boxes show the BKF11 and KF13 samples, blue circles show the C14 sample of C-COSMOS X-ray detected ETGs. Triangles pointing down represent upper limits.

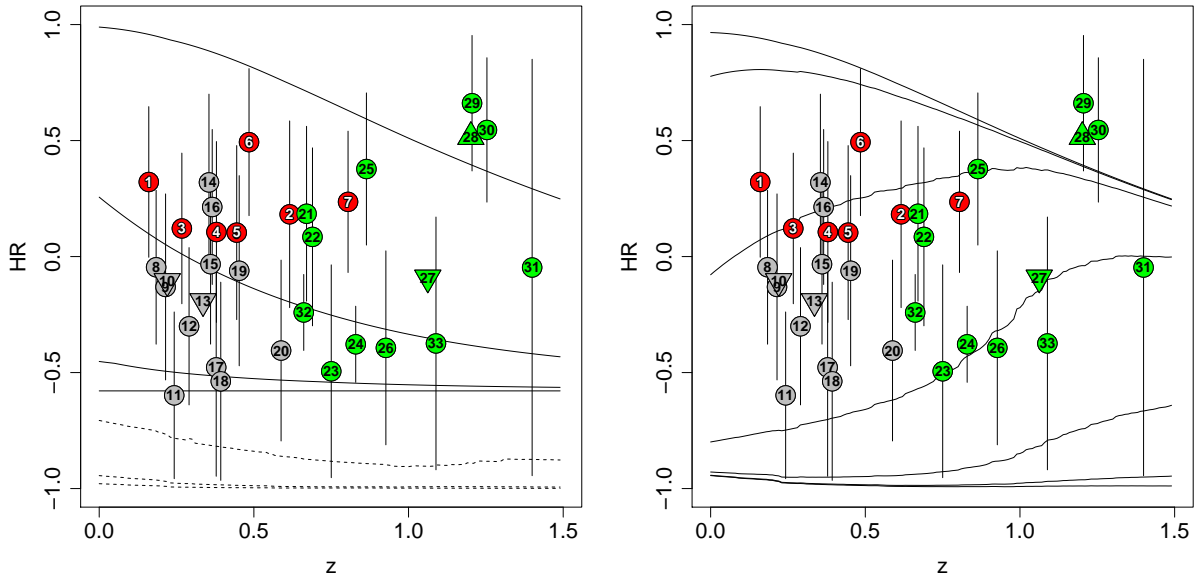


Fig. 6.— Left: HR- z scatter diagram of L_K -first bin. Triangles pointing up and down represent lower and upper limits on HR, respectively. Dashed lines show HRs expected from thermal models (APEC) with increasing temperature from bottom to top 0.7, 1, 2 and 3 keV. The full lines represent simulated HR from power-law models with fixed slope $\Gamma = 2$ and increasing intrinsic absorption from bottom to top 0, 10^{21} , 10^{22} and 10^{23} cm^{-2} . Right: Same as left panel, but for models comprising a thermal model with temperature of 1 keV plus a power-law with fixed slope $\Gamma = 2$ and intrinsic absorption of 10^{23} cm^{-2} . The relative normalization of the two models is, from top to bottom, 10^{-3} , 10^{-2} , 10^{-1} , 1, 10, 10^2 and 10^3 , corresponding to a contribution of the power-law component to the total flux of $\sim 0.2\%$, $\sim 2\%$, $\sim 15\%$, $\sim 62\%$, $\sim 94\%$, $\sim 99\%$ and 100% , respectively.

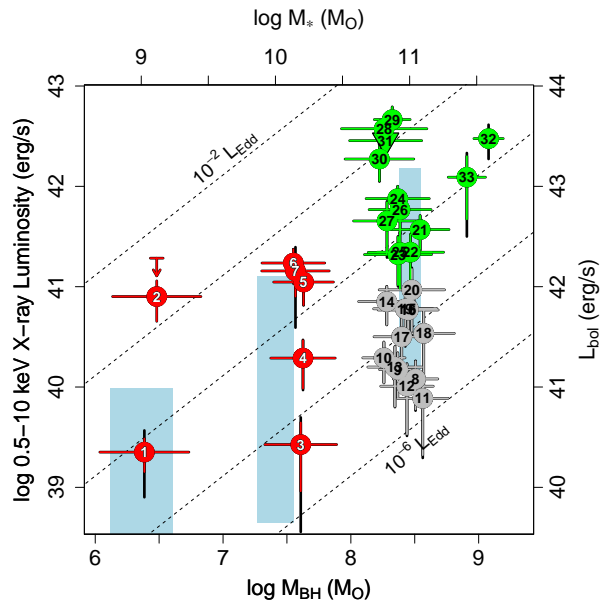


Fig. 7.— X-ray luminosity (after LMXBs subtraction) versus black hole mass M_{BH} (evaluated from M_* according to the [McConnell & Ma 2013](#) relation) for the L_K -first stacking bins. The stellar mass M_* from COSMOS catalog is plotted on the top axis. Lines of constant L_{bol}/L_{Edd} , given M_{BH} and L_{bol} , are shown as diagonals (from bottom to top 10^{-6} , 10^{-5} , 10^{-4} , 10^{-3} and 10^{-2}). The bins are color-labeled as in Figure 3. Light blue boxes represent the predictions of the [Volonteri et al. \(2011\)](#) models for $M_* = 10^9 M_\odot$, $10^{10} M_\odot$ and $10^{11} M_\odot$, where the top of each box refers to radiatively efficient accretion flows and the bottom refers to RIAFs.